# Effect of Acoustic Radiation Force on Displacement of Nanoparticles in Collagen Gels

Mia Kvåle Løvmo*, Petros Tesfamichael Yemane*, Astrid Bjørkøy, Rune Hansen, Robin Cleveland, Bjørn Angelsen, Catharina de Lange Davies

***Abstract*—Penetration of nanoscale therapeutic agents into the extracellular matrix (ECM) of a tumor is a limiting factor for sufficient delivery of drugs in tumors. Ultrasound in combination with microbubbles causing cavitation, is reported to improve delivery of nanoparticles (NPs) and drugs to tumors. Acoustic radiation force (ARF) could also enhance the penetration of NPs in tumor ECM. In this work, a collagen gel was used a model for tumor ECM to study the effect of ARF on the penetration of NPs as well as deformation of collagen gels applying different ultrasound (US) parameters (varying pressure and duty cycle). The collagen gel was characterized, and diffusion of water and diffusion of NPs measured. The penetration of NPs into the gel and was measured by confocal laser scanning microscopy and numerical simulations was performed to determine the ARF and to estimate penetration distance and extent of deformation. ARF had no effect on the penetration of NPs into the collagen gels for the US parameters and gel used, whereas a substantial deformation was observed. The width of the deformation on the collagen gel surface corresponded to the US beam. Comparing ARF caused by attenuation within the gel and Langevin pressure caused by reflection at the gel-water surface, ARF was the dominant mechanism for the gel deformation. The experimental and theoretical results were consistent both with respect to NP penetration and gel deformation.**

***Keywords* — collagen gel; extracellular matrix; ultrasound; nanoparticles; drug delivery; acoustic radiation force; acoustic radiation pressure; acoustic streaming**

## I. Introduction

Encapsulation of therapeutic agents into nanoparticles (NPs) has been shown to enhance the accumulation of drugs in tumors compared to administration of free drugs and to reduce the toxic effects toward normal tissue [1]. This is probably due to the Enhanced Permeability and Retention (EPR) effect, i.e. the hyperpermeable tumor vessels and lack of functional lymphatic vessels [2]. Although the accumulation of drugs is increased, it is still low [3], and NPs are heterogeneously distributed in the extracellular matrix (ECM), mainly located close to the vessel wall [4], thus the drug treatment becomes in-sufficient.

Focused ultrasound (FUS) has been reported to improve the tumor uptake of NPs and improve the distribution of NPs throughout the ECM [5]. Cavitation is an important and well-studied mechanism in the field of drug delivery [6, 7]. However, acoustic radiation force (ARF) could also be a mechanism for local enhanced drug delivery. ARF is the transfer of momentum to the tissue from the US wave due to absorption and scattering of the wave. The ARF results both in displacement of particles and tissue [8]. In addition, ARF acting on a fluid medium results in a flow known as acoustic streaming [9] which may increase the drug transport in tissue. ARF has also been reported to push microbubbles circulating in the blood stream towards the vessel wall [10-14], to induce shear forces, which can open gaps in endothelium of the vessel wall, to widen the intercellular space [15], and to expand the extracellular and perivascular spaces in the brain [16].

The present study aims to develop an *in vitro* model to study mechanisms behind US enhanced delivery of NPs. *In vitro* models are important supplements to *in vivo* studies. Collagen gels were used as collagen is the major structural component of the ECM, and collagen gels have similar mechanical properties and porous structures as ECM [17]. Structural and mechanical properties of the collagen gels were determined. Collagen gels containing NPs were exposed to different US parameters using

This work was funded by The Research Council of Norway project number 240316.

M. K. Løvmo, P.T. Yemane, A. Bjørkøy, A, and C.de L. Davies are with Department of Physics, The Norwegian University of Science and Technology (NTNU), Høgskoleringen 5, 7491 Trondheim, Norway (email: Catharina.davies@ntnu.no).

R. Hansen, and B. Angelsen are with Department of Circulation and Medical Imaging, The Norwegian University of Science and Technology (NTNU), P.O. Box 8905, 7491 Trondheim, Norway. R.Hansen is also with Department of Health Research, SINTEF Digital, Trondheim, Norway.

R. Cleveland is with the Institute of Biomedical Engineering, University of Oxford, United Kingdom.

*M. K. Løvmo and P. T. Yemane contributed equally to this work.

a focused 10 MHz US transducer. The penetration of the NPs into the gel and deformation of the gel were imaged using confocal laser scanning microscopy (CLSM). To further understand the experimental results, the theoretical magnitude of the ARF was estimated using the experimental US parameters, and the deformation of the collagen gel due to ARF was estimated.

## II. Materials and Methods

### A. Collagen gel preparation

Collagen solutions were prepared from rat-tail CORNING® COLLAGEN I, High Concentration (8 - 11mg/mL) (BD Biosciences, San Jose, CA, USA), following the manufacturer's protocol. In brief, collagen solutions were prepared by mixing concentrated collagen with 10X concentrated phosphate-buffered saline (PBS) (Sigma-Aldrich, St. Louis, MO, USA) to a concentration of 2.5 mg/ml. Collagen solutions were pH adjusted to 7.2 ±0.2 by adding 1M sodium hydroxide. Before mixing all components, they were kept on ice for at least 30 min, and after mixing they were kept at 37°C for 40 min to polymerize. A collagen-NP solution was made by adding NPs to the collagen solution at a NP concentration of 120 µg/mL and vortexing thoroughly.

A two-layered *in vitro* collagen gel was made for studying penetration of NPs into a model for tumor ECM. The collagen-NP gel was combined with the collagen gel prior to gelling. A 2 mm diameter and 1 mm deep silicone well (Grace Bio-Labs Press-To-Seal silicone isolator, PSA one side, Sigma-Aldrich, St. Louis, MO, USA ) was centered and attached to the bottom of one well of a µ-slide 8 well chamber slide with grids (Grid-500 ibidi®, Thermo Fisher Scientific Inc., Pittsburg, PE, USA). 7 µL of 2.5 mg/mL collagen solution was pipetted into the silicone well. 7 µL of 2.5 mg/mL collagen-NP solution was pipetted on a 5 x 5 mm glass coverslip. The coverslip was flipped upside down and pressed gently onto the silicone well to combine the collagen-NP solution with the collagen solution. The well plates were immediately lidded, inverted (to avoid sedimentation of NPs during gelling) and incubated at 37°C for 40 min to polymerize. Then, the collagen models were stored inverted at 4°C and used for experiments within 12 hours. Right before use, the well plates were inverted again, the coverslip on top was gently removed, and the gel was covered with 400 µl PBS before a pre- US image was acquired with CLSM as described below.

### B. Synthesis and characterization of NPs

The PEGylated poly(2-ethyl-butyl cyanoacrylate) (PEBCA) NPs were synthesized by miniemulsion polymerization as described previously [18]. The NPs used in this study were loaded with the fluorescent dye NR668 (modified NileRed [19], custom synthesis, 0.5 wt%) by addition to the oil phase of the miniemulsion. For PEGylation of the NPs, Brij L23 (10mM, 23 PEG units, MW 1225, Sigma-Aldrich, Oslo, Norway) and Kolliphor HS15 (10mM, 15 PEG units, MW 960, Sigma-Aldrich, Oslo, Norway) were added to the aqueous phase of the miniemulsion. For more details see [18, 20]. The size, polydispersity index (PDI) and the zeta potential of the NPs were measured by dynamic light scattering (DLS) using a Zetasizer Nano ZS (Malvern Instruments, Malvern, UK). The z-average diameter was in the range of 140-195 nm, PDI was less than 0.2, and the zeta-potential was in the range of -1 to -2.5 mV. PEGylation of the NPs were quantified by $^1$H nuclear magnetic resonance (NMR) as described elsewhere [21] and 41.4 ethylene units per nm$^2$ was measured.

### C. Characterization of collagen gels

#### 1) DW-MRI

Diffusion-weighted Magnetic Resonance Imaging (DW-MRI) was performed on one-layer collagen gel. A µ-slide of 8 wells was filled with 684 µL of gel per well. DW images were acquired on a 7T Bruker Biospec (Bruker Biospin, Ettlingen, Germany) with a 72 mm volume resonator for RF transmission and a quadrature mouse brain surface coil for reception [22]. The images were acquired as explained in [22] by the following settings: spin echo (SE) planar imaging (EPI), echo time (TE) = 28ms, repetition time (TR) = 3000 ms, 4 segments, NA=4, matrix size = 64 x 64, b-values = 100, 300, 600 and 1000s mm$^2$, diffusion gradient separation time=14 ms, diffusion gradient duration = 7 ms, three orthogonal gradient orientations (and fat suppression, for tumor comparison values). The Apparent Diffusion Coefficient (ADC) maps were computed using in-house software developed in MATLAB (Mathworks Inc., Natick, MA, USA). For each voxel, the logarithm of the signal intensity vs b-value was fitted linearly to obtain ADC value for each gradient direction, followed by averaging over the three gradient directions to obtain mean ADC maps. The median ADC for each gel was calculated for the entire gel.

#### 2) Measurements of the Young modulus using indentation

The Young modulus of one-layer collagen gel was estimated using a custom built macroindenter. The indenter with a 2.25 mm radius spherical tip, was mounted onto a single-axis stepper motor (TRB25CC, Newport, Irvine, CA,USA) (travel range 0 – 25 mm, minimum increment 0.1 µm), connected to a motion controller (SMC100CC, Newport, Irvine, CA,USA). Force was recorded using a load cell (WZA2244-N, Sartorius, Gottingen, Germany) (max load 220 g, resolution 0.1 mg.). All tests were performed on gels in a well (18 mm in diameter and 2 mm height). The force and z-position of the indenter were recorded at an indentation speed of 40 µm/s. The gel was compressed by about 10-15% of its thickness, to minimize the effects from the bottom of the well. A series of 5–6 indentations were performed at different locations on the gel. Three different gel samples were tested.

The Hertz contact model was used to obtain the elastic modulus from the load-indentation depth curves [23]. For a spherical indenter of radius R, force-displacement curve is given by [23, 24]:

$$F = \frac{4}{3} E^* \sqrt{Rh} * h \quad (1)$$

where $E^*$ is the reduced modulus of the collagen gel, R is the radius of the indenter tip, h is the distance of the indenter into

the collagen gel surface and F is the force measured by the load cell. For two elastic bodies in contact (indenter and gel), the reduced modulus $E^*$can be obtained from Hertz contact theory [23]:

$$\frac{1-\nu^2}{E} = \frac{1}{E^*} - \frac{1-\nu_i^2}{E_i} \quad (2)$$

where $\nu$ is the Poisson's ratio and E is Young's modulus of the gel, and $\nu_i$ and $E_i$ those of the indenter. Approximating the collagen gel as an incompressible material [24], the Poisson ratio ($\nu$) is 0.5. For the indenter tip made of Teflon, $E_i$ = 0.5 GPa and $\nu_i$ = 0.41 [25]. The Young modulus of the collagen gel was determined by fitting Eq. (1) to the experimental data to get E* and using Eq. (2) to estimate E.

*3) Deformation of Collagen gel by indenter*

The inelastic response of the gel was also assessed with the indenter. One-layer collagen gel was placed in a container as described above, and 40 µl of PBS was added on top of the gel to prevent drying. The indentation parameters used were the same as described above. The macroindenter compressed the collagen gel reducing its thickness 10-15%, and the indenter compressed the gel for 10 min before being unloaded. Ten min holding time was applied to be consistent with the total sonication time used experimentally. Immediately after unloading, the gel was loaded again at the same position and immediately unloaded. In both cases, the load and displacement of the indenter were recorded. From the force-distance curve of the two indentations, the difference in the contact point between tip and collagen surface was computed, describing how much the gel was deformed during the first indentation. Six different collagen samples were used, and each sample was indented at 3-5 different positions.

*4) Diffusion of NPs in collagen gels*

Diffusion of NPs in one layer collagen-NP gel (300 µL) was measured by CLSM and Raster Image Correlation Spectroscopy (RICS) as described previously [21] and analyzed as in [26]. An inverted LSM 510 (Carl Zeiss, Oberkochen, Baden-Württemberg, GE) and HeNe laser was used. The collagen network was imaged by CRM, using a HeNe laser (543 nm) and a 500-550 nm band-pass filter. NP fluorescence was detected using a 560 nm long pass filter. Time series of CLSM images were obtained by consecutive images (frames) of NPs in the gel. For every experiment, 8 or 15 frames (512x512 pixels) at minimum 8 locations in the gel, were collected. The scanning speed along the fast scanning axis was 51.2 µs/pixel and the scanning step corresponding to one pixel was 54.9 nm. The estimated number of NPs per confocal volume and the diffusion coefficients of the NPs were calculated with the RICS Manics software. The mean and standard deviation (SD) of the diffusion coefficient are weighted by the number of particles per confocal volume. The experiment was performed three times with new gels. RICS analysis was also performed as above for NPs in PBS solution (n=3).

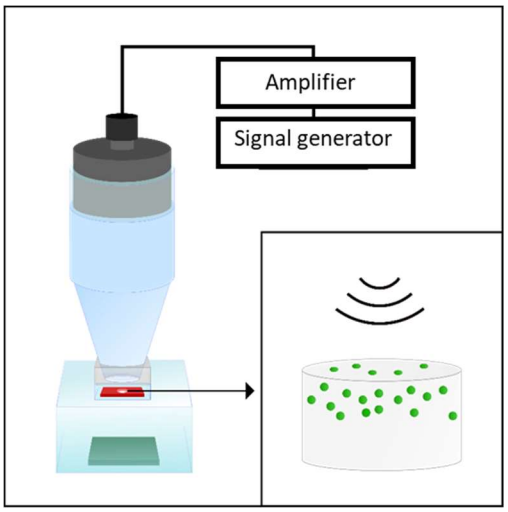


**Figure 1:** Schematic illustration of the US exposure setup and the resulting collagen gel model with NPs (green) confined in the top layer of the model.

## D. US set-up and treatment

A single-element, FUS immersion transducer (center frequency: 10 MHz, focal depth: 50 mm, diameter: 19 mm, S-series; Harisonic, Besancon, France) was driven by an arbitrary waveform generator (33500B, Agilent Technologies, Santa Clara, CA, USA) through a 50-dB power amplifier (2100L, E&I, Rochester, NY, USA). Characterization of the transducer was performed in an Acoustic Intensity Measurement System (AIMS III, Onda, Sunnyvale, CA, USA), filled with degassed water, using an HGL-0200 capsule hydrophone with anAG-2010 pre-amplifier and analyzed with Soniq Software (Onda, Sunnyvale, CA, USA). The -3 dB and -6 dB beam widths at foci had diameters of 0.34 mm and 0.52 mm respectively. The transducer was placed in a custom-made cone filled with degassed distilled water and sealed with an acoustically transparent parafilm membrane (Bemis Company Inc., Neenah, WI, USA). The cone was gently placed into a hole in the middle of the well plate lid, the excess PBS was pushed away without generating air bubbles and the cone was held in place by a 3D positioning arm. The well plate was placed on a platform holding the bottom of the plate in a degassed water bath with acoustic absorbers at the bottom to minimize standing waves. US treatment was given from above (Figure 1).

The US parameters were chosen to deliver less than 6.1 W, which was the maximum effect to be used to avoid heating and damage of the transducer according the manufacturer. US exposure were changed as a function of 1) pressure and 2) duty cycle;

1) Three acoustic pressures (peak negative pressures) of 2.2, 2.7 and 3.0 MPa at focus were applied, with 0.5 µs pulse length and 66 kHz pulse repetition frequency (PRF) resulting in a duty cycle of 3.3%.

2) Three different pulse lengths of 23.3, 46.7 and 93.3µs were used at 2.2 MPa and PRF of 1 kHz resulting in 2.3, 4.7 and 9.3% duty cycles respectively. All US treatments had a duration of 10 min and experiments were performed three times for each combination of parameters.

### E. Confocal imaging of collagen model

The distribution of NPs in 2-layered collagen gels were imaged by CLSM (TCS SP8, Leica, Wetzlar, GE) to generate z-stack of the gel before and after US exposure. The same imaging procedure was performed for control experiments, placing the collagen gel in the US exposure setup, but no US was applied. In sequential scans, a White Light laser (WLL) at 471 nm was used to excite NR668-labeled NPs and fluorescence was detected at 560-650 nm, and collagen fibers were imaged by CRM with a 464-477 nm band-pass filter in front of the detector. A 25X/0.95 water immersion objective was used. Tile scans of the middle 1.36 x 1.36 mm of the gel were obtained by stitching 6x6 images together in the Leica LASX hardware. The images were captured using a frame size of 512x512 pixels (233 x 233 µm) at 600 Hz scan speed. A tile scan z-stack was generated by capturing these tile scans every 10 µm from the bottom of the ibidi grid slide to the top surface of the gel, generating a 3D image stack (a tile scan z-stack) of both the fluorescence channel and the reflection channel. An optical section of 11.8 µm was used. All samples had a thickness of 950 ± 50 µm, giving rise to z-stacks of around 100 tile scans. The laser intensity and detector gain were kept the same for all samples, and were set to minimize noise and utilize the grey scale. More detailed image of collagen fibers and NP distribution were acquired at higher zoom factors throughout the gel. To visualize the collagen fibers and the NP distribution at the boundary between collagen-NP and collagen only, a volume of 38x38x80 µm (w x l x h) selected at the boundary between the two layers in the model from a 3D image stack and a 3D volume was reconstructed in Amira Software [27].

### F. Image processing and quantification of NP penetration

The tile scan z-stacks were processed in ImageJ (National Institutes of Health, Bethesda, MD, USA) to quantify the NP fluorescence as a function of penetration into the collagen gels. The US exposure had caused a circular indentation on the gel surface, and in the post US images, a circular ROI of 300 µm diameter was selected in the center of the indent to analyze a region that had received US treatment above the -3dB acoustic pressure. The mean intensity in the ROI was calculated as a function of distance into the gel, in both channels of the z-stack pre and post US treatment. The same size area was selected in the center of the z-stacks obtained from the control experiments and the same calculation was performed.

The obtained data from ImageJ was imported to MATLB (MathWorks Inc., Natick, MI, USA) for further analysis and plotting. Representative fluorescence intensity profiles obtained before and after US exposure are plotted together in Appendix C, Figure S1a. The displacement of the post-US intensity profile relative to pre-US profile was quantified as following: The surface of the gel was defined at the position where the fluorescence intensity had increased to half of maximum value. The interface between NP-collagen gel and collagen gel was defined at the position in the gel where the fluorescence intensity decreased to half of maximum value. The displacement through the NP-collagen gel was estimated from characteristic peaks in the fluorescence intensity profile as indicated in Appendix C, Figure S1a, and these displacements were plotted as a function of position in the gel in Appendix C, Figure S1b. An exponential curve was fitted to the data.

### G. Statistical analysis

One-way ANOVA tests were carried out to evaluate statistically significant differences between treatment groups (SigmaPlot 13.0, Systat Software Inc., San Jose, CA, USA). Differences between treatments were considered statistically significant for $p < 0.05$. All experiments consist of three replicates and the results are expressed as mean ± SD, unless otherwise is specified.

### H. Simulation of pressure, ARF and displacement of the gel and NPs

ARF was simulated using the experimental US input parameters to obtain information about the magnitude of the ARF and possible displacement of NPs into gels as well as the deformation of the collagen gel caused by the US beam. Both ARF attenuation and radiation pressure were considered (Figure 2).

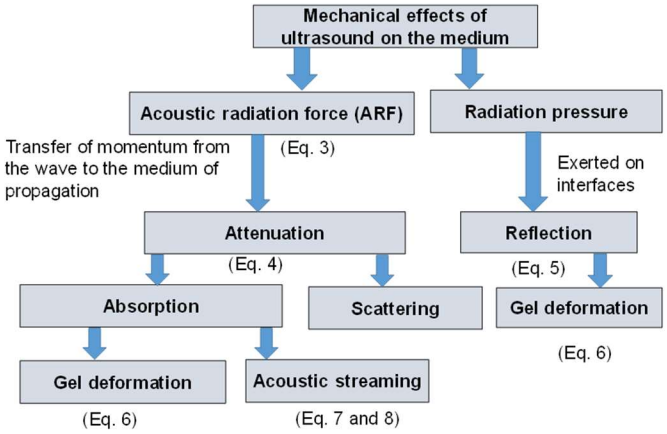


**Figure 2:** The flow chart showing the physical processes on the gel surface and in the gel induced by ARF and the radiation pressure. The equations used to calculate ARF, attenuation, reflection and gel deformation and acoustic streaming are indicated.

#### 1) ARF estimation

The ARF is given by the transfer of momentum from the wave to the medium of propagation, where the pressure and particle velocity become out of phase, and is proportional to the average intensity of the wave and the attenuation of the medium [28]. To account for the frequency dependence of the attenuation in the medium, the ARF per unit volume ($\Delta V$) can be expressed as (see Appendix B) [29, 30]:

$$\frac{\Delta F_r(r,\omega)}{\Delta V} = \frac{1}{2\pi T_p \rho c^2} \int \alpha(r,\omega)|P(r,\omega)|^2 \, d\omega \qquad (3)$$

where r, w, $\rho$ ,c and $T_p$ are position, angular frequency, mass density, speed of sound and pulse duration, respectively. α(r, $\omega$) is the attenuation and is given by the sum of absorption and scattering, and $P(r, \omega)$ is the Fourier transform of the pressure at the point $r$.

Acoustic attenuation in biological tissue follows a power law frequency dependence in the form of:

$$\alpha(f) = \alpha_0 (\frac{f}{f_0})^b \quad (4)$$

where $\alpha_0$ is the attenuation constant at $f_0$, $f$ is the frequency in MHz, $f_0$ is usually 1 MHz, and $b$ is the frequency-power law exponent. Typically, b is in the range of $1 \leq b \leq 1.6$ in most biological tissues and 2 in water [31].

As shown by Eq. (4), ARF is a function of the attenuation and intensity. In order to obtain high amplitude of ARF and induce effective transport of the objects, the amplitude of the ultrasonic excitation should be high enough to excite the nonlinear effects. Eq. (5) shows that the harmonics are more strongly attenuated by the medium than the fundamental. To calculate the ARF in an irradiated medium using Eq. (4), the pressure $P(r, \omega)$ was first calculated using an existing simulation software, HIFU simulation [32], which is based on the KZK equation. Then, the ARF was computed using a custom-written script in MATLAB (Mathworks Inc., Natick, MA, USA). In the simulations of ARF, water was used as the propagation medium for the first 51.6 mm followed by the thickness of the collagen gel. The parameters for water were: $\alpha_0$ = 0. 025 Np/m [31], $b$ = 2, $c$ = 1482 m/s, density $\rho$ = 1000 kg/m$^3$, and nonlinearity parameter (B/A) = 4.96 [33] and for collagen gel: $\alpha_0 = 0.18$ Np/m [34], $b = 1.6$ [34], c = 1496 m/s [35], $\rho$ = 1116 kg/m$^3$ [35] and B/A = 7.43 (B/A of muscle [33] due to lack of experimental data for collagen gel). The surface transducer pressures used as input parameters in simulation of the ARF were determined as described in Appendix A, and found to be 105, 146 and 206 kPa for peak negative pressures of 2.2, 2.7 and 3.0 MPa.

A radiation pressure will also be exerted on interfaces where there is a reflection associated with impedance differences, termed Langevin radiation pressure. The net force per unit area on an interface ($P_R$) between two media with different acoustic properties is given by [36]:

$$P_R = (1 + R^2 - \frac{c1}{c2}(1 - R^2)) \frac{<{P_I}^2>}{\rho_1 {c_1}^2} \quad (5)$$

where, $R = \frac{Z_2 - Z_1}{Z_2 + Z_1}$ is the pressure reflection coefficient, $z_1$, and $z_2$ are the acoustic impedance of medium 1 and medium 2, respectively, $c_1$, and $c_2$ are the speed of sound in medium 1 and medium 2, respectively, and $P_I$ is the RMS pressure in the incident US beam.

Assuming uniform pressure ($P_L$), with radius a, on an elastic half space, the deformation at the interface ($\delta$) is given by [37, 38]:

$$\delta = 2 * P_L a \frac{1 - \nu^2}{E} \quad (6)$$

where, $\nu$ is the Poisson's ratio of the material, and E is Young's modulus of the material. The total US induced deformation of the material is due to a combination of the ARF resulting from the material is due to a combination of the ARF resulting from gel attenuation and Langevin pressure resulting from reflection at the water-gel interface. The ARF load was estimated from Eq.3 and multiplied by $\pi a^2 h$, (assuming cylindrical configuration). $a$ is half of the beam width and h is thickness of the gel. The whole thickness of the gel was used because the absorption length is longer than the gel thickness. The Langevin surface pressure was estimated by Eq. 5 and multiplying with the area $\pi a^2$.

*2) Displacement of NPs due to acoustic streaming*

The attenuation of the US wave produces an ARF on the NP and the fluid in which the NP is suspended. NP motion is induced because of entrainment by the moving fluid depending on the NP's size, density and surface characteristics [39, 40]. Hence, NPs may be transported through the interstitium if the NPs can move freely with the fluid, i.e. if the pore diameter of the interstitial space is larger than the particle size. By modelling the interstitium as a porous medium [17, 41], the velocity of the fluid can be calculated by Darcy's law:

$$U(r) = \frac{K \nabla P}{\mu} = K' \nabla P \quad (7)$$

where $U$ is the fluid velocity, K is the specific permeability, μ is the dynamic viscosity, K' is the hydraulic conductivity of the interstitium [42] and ∇P is the pressure gradient on the medium that is the driving force for the fluid. The mean dynamic viscosity of collagen gel (2.5 mg/ml) has been reported to be 7.96 Pa·s [43], and specific permeability of collagen gel (3.5 mg/ml) ranges from $10^{-14}$ to $10^{-13}$ m$^2$ [44] and for a concentration of 1.5 mg/ml, a mean value of 7.67 x $10^{-13}$ m$^2$ is reported [45]. Therefore, the hydraulic conductivity (K') for collagen gel (2.5 mg/ml) ranges from approximately 1.25 x $10^{-15}$ m$^4$N$^{-1}$s$^{-1}$ to $10^{-13}$ m$^4$N$^{-1}$s$^{-1}$. Assuming ARF is the only unbalanced force acting on the medium, $\nabla P = \Delta F_r / \Delta V$. The displacement of the NPs can be estimated as:

$$\psi_{ps} = U T_{on} = K' \frac{\Delta F_r}{\Delta V} T_{\text{on}} \quad (8)$$

where $T_{\text{on}}$ is the total time the particle was exposed to the ARF. For a pulsed excitation $T_{\text{on}} = DC \cdot T_{\text{tot}}$, $DC$ is the duty cycle and $T_{\text{tot}}$ is the total scanning time.

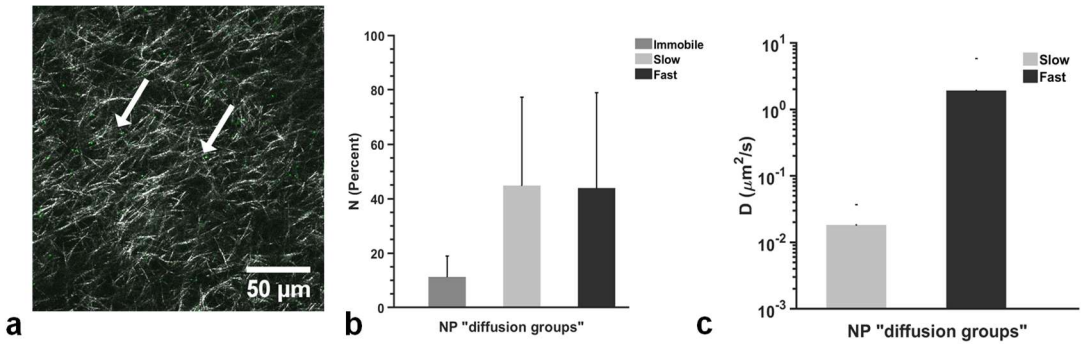


**Figure 3:** Diffusion of NPs in collagen gel. a) Overlay image of reflection and fluorescence channel showing collagen fibers (white) and NPs (green) Some NPs are indicated by the arrows. b) Percentage of NPs in each population of immobile, slow and fast diffusing NPs with SD (n=3). c) The corresponding average diffusion coefficient for the slow and fast diffusing populations with SD all analyzed particles.

## III. Results

### A. Characterization of collagen gels

#### 1) Young's modulus of collagen gels

The Young modulus was determined from indentation data, and the Hertz contact model was fitted to the experimental data. A representative experimental indentation curve and the corresponding fitting are shown in Appendix D, Figure S2. The Young modulus was found to be E=0.24 ± 0.02 kPa (mean of 3 independent experiments).

#### 2) DW-MRI

The diffusion of water in the gel was measured and compared to ADC values in tissue. The ADC value of water in 2.5 mg/ml collagen was 1.83 x $10^{-3}$ $mm^2$ $s^{-1}$ which is of the same order of magnitude as ADC values found for tissues, 0.6 x $10^{-3}$ $mm^2$ $s^{-1}$ to 1 x $10^{-3}$ $mm^2$ $s^{-1}$ [46].

#### 3) Diffusion of NPs in collagen gels

A CRM image of the collagen network and fluorescent NPs is shown in Figure 3a. RICS and image analysis of NPs diffusing in collagen gels revealed a multimodal diffusion behavior that could be divided into three distinct populations of NPs: fast diffusing, slow diffusing and immobile.

The percentage of NPs within the three "diffusion groups" and their diffusion coefficients are shown in Figure 3b and c, respectively. The percentage of fast and slow diffusing NPs were 44 ± 35% and 45 ± 32% respectively, and the remaining 11 ± 8% were immobile. The diffusion coefficient for the fast and slow diffusing NPs were 2 ± 4 $\mu m^2/s$ and (2 ± 2)x $10^{-2}$ $\mu m^2/s$, respectively. The diffusion coefficient of NPs in PBS was measured to be 2.4 ± 1.3 $\mu m^2/s$, which is consistent with the Stokes-Einstein relation (calculated to 2.4 $\mu m^2/s$ at 20 ºC in water). Thus, the diffusion coefficient of the fast diffusing NPs in collagen gel is not significantly different from the diffusion coefficient of NPs in water.

### B. Two-layered collagen tissue-mimicking model

A two-layered collagen gel with NPs and collagen in the upper layer and collagen only below, were used as a model for tumor ECM. A high concentration of NPs is often observed close to the blood vessel wall [4] and the upper collagen-NP layer represented this NP distribution and the NPs could penetrate into the collagen layer below. A CLSM image of a XZ-cross section of the two layers are shown in Figure 4, and further described in the supplementary (see Appendix E, Figure S3). The intensity profile of the collagen is shown in Figure S3d. The continuous intensity profile shows that the collagen network is continuous also at the interface between the two layers.

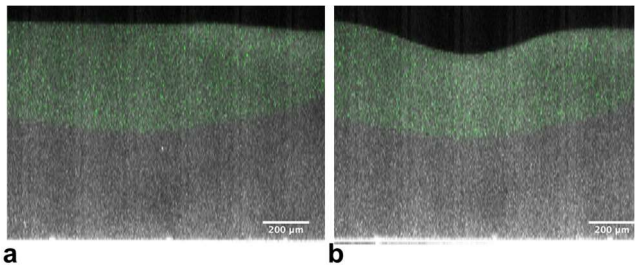


**Figure 4:** US induced displacement of the collagen gel. a) Before US b) After US exposure. XZ cross sections were imaged from the surface of the gel to the bottom.

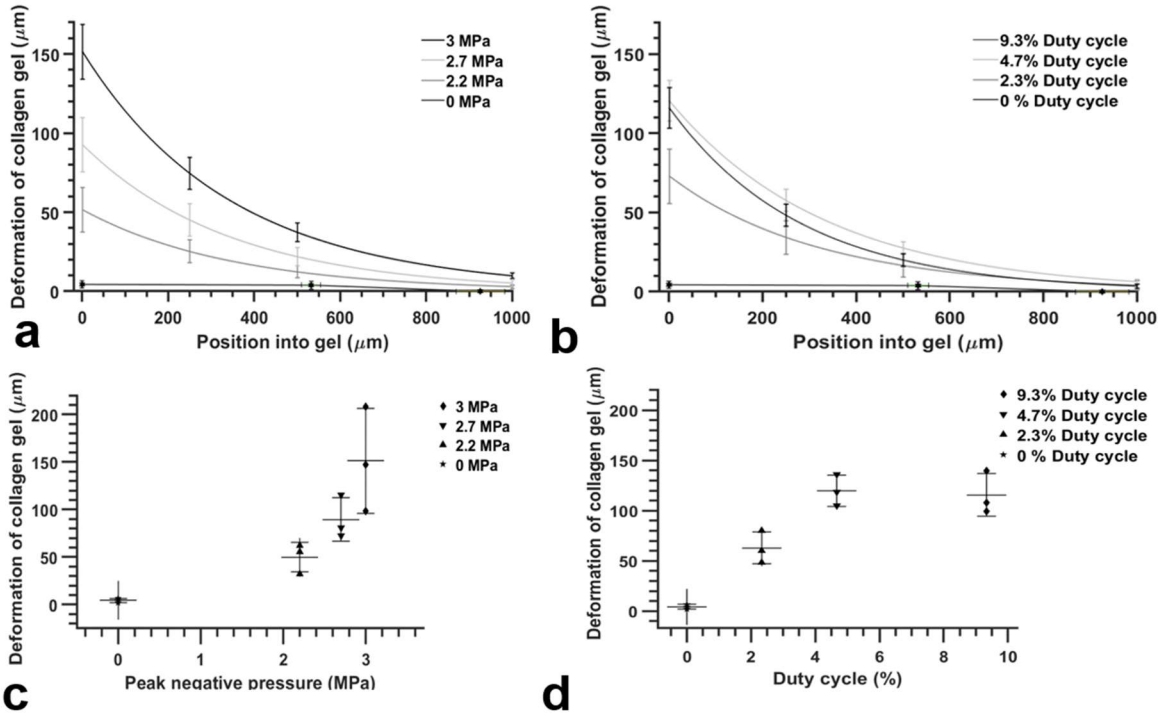


**Figure 5:** Deformation of collagen gel after US exposure comparing pre and post US images. a) and b) show the mean deformation of the gel as a function of position into the gel for US treatment groups with varying acoustic pressure and duty cycle, respectively. Exponential curves were fitted to the experimental data for 3 experiments at the 3 different US exposures, and panel a) and c) show the mean of the 3 fitted curves with the SD. c) and d) show the deformation of collagen gel at the surface for the variable acoustic pressure and duty cycle, respectively. The data points are the mean of 3 experiments with SD.

### *C. Displacement of NPs and collagen gel by US*

Z-stacks of images acquired before and after US exposure in the center region of the gels were analyzed to detect a change in NP penetration into the gels. In Figure 5, clearly visible changes from the pre image (Figure 5a) of the gel to the post US exposure image (Figure 5b) show that the US exposure induced a deformation on the gel. The width of the deformation on the gel surface corresponded to the US beam. The NP fluorescence intensity decreased steeply at the interface between the two gel layers (see Appendix E Figure S3e) and no NP fluorescence was detectable in the lower collagen gel. This indicates that the observed shift in fluorescence intensity profile is due US-induced displacement at the gel surface and US had no detectable effect on NP penetration in the gel.

The displacement of the gel was determined by comparing the fluorescence intensity profiles before and after the US exposure. This displacement seemed to decrease exponentially as a function of position into the gel. The experimental data and the exponential fitted decay curves are shown in Figure 5. The mean US-induced gel displacement as a function of position into the gel is shown for the three peak negative acoustic pressures using a duty cycle of 3.3% (Figure 5a) and for the three duty cycles using peak negative pressure of 2.2 MPa (Figure 5b). The gel displacement increased with increasing peak negative pressure (Figure 5c) as well as duty cycle (Figure 5d).

The deformation (Figure 5c) showed that an increase in peak negative acoustic pressure from 2.2 to 2.7 MPa lead to an increased mean gel deformation from 50 ± 16 μm to 90 ± 23 μm. A further increase to 3.0 MPa resulted in a mean displacement of 151 ± 55 μm. Increasing the duty cycle from 2.3% to 4.7% (Figure 5d) increased the displacement from 63 ± 16 μm to 120 ± 16 μm. A further doubling of the duty cycle to 9.3% lead to a gel displacement of 116 ±21 μm, which was not significantly different from 4.7% duty cycle. Hence, a

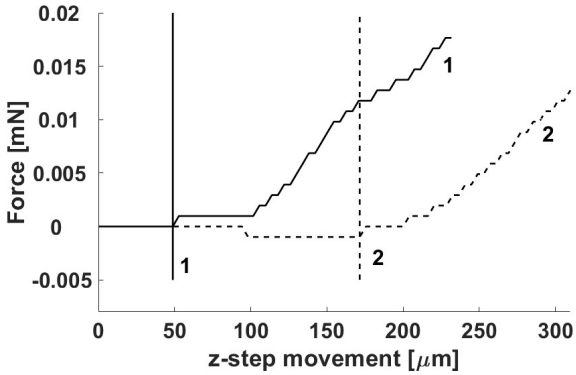


**Figure 6:** Representative figure of force-displacement curves generated using a spherical tipped indenter with 2.25 mm radius loaded at 0.4 mm/s. The contact points to the gel for the two indentations curves are indicated. 1 (solid line) is the loading curve hold for 10 min, and 2 (dashed line) is the subsequent loading curve.

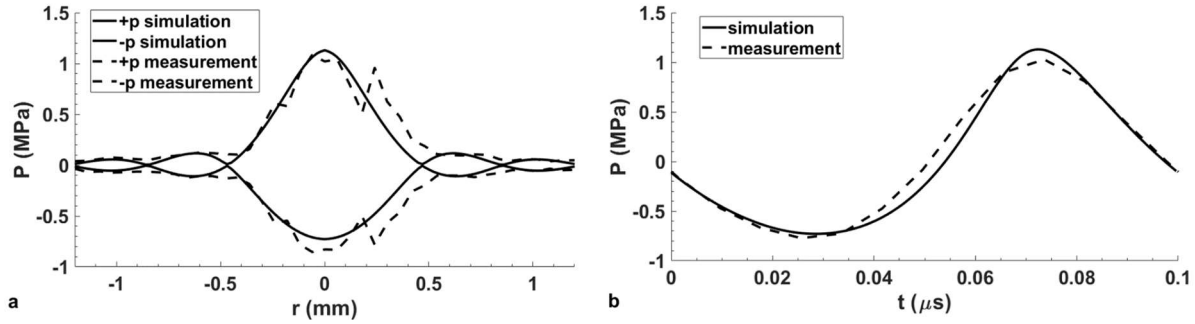


**Figure 7**: Radial peak pressures (a) and waveform (b) at the focus of the transducer (50 mm). Experimental values and HIFU simulation. Input pressure on the surface of the transducer is 25 kPa.

maximum level of 120 ± 16 μm displacement was found for the duty cycle parameters investigated. The control gels have a close to zero gel displacement from pre to post image acquisition (4 ± 2 μm).

### *D. Deformation of the collagen by indenter*

The US-induced deformation of the gel was compared to a mechanical load caused by the macroindenter onto the gel surface. A representative force-displacement curve is shown in Figure 6. From the force-distance curve of the two subsequent indentations, it is clearly seen that the contact position of the indenter tip onto the surface of the collagen gel is different, i.e. position 1 and 2 in Figure 6. Mean displacement of 155±44 μm was found after the collagen was compressed 10-15% of its thickness using an indenter load in the range of 0.01-0.02 mN which was held for 10 min before unloading. This displacement corresponds to the experimental gel deformation (151 ± 55 μm) induced by the highest US pressure applied (Pneg=3.0MHz in Figure 5a).

### *E. Simulation: Pressure, ARF and displacement of the gel and NPs*

#### *1) Pressure and ARF*

In order to predict the acoustic field generated by the US, simulations were performed using the experimental parameters. The simulation was first validated with an experiment using the lower-source pressure on the transducer (25 kPa) to avoid damage to the hydrophone. The measurement was done in a water tank filled with degassed and distilled water with a calibrated hydrophone. Figure 7 compares the focal waveform and radial distribution of the peak positive and negative pressures. There is good agreement between simulated and experimental results.

The ARF was simulated, and Figure 8 shows axial peak positive and negative pressures and the axial ARF as a function of depth for the first 51.6 mm of water and into a collagen gel. From the simulation, for the transducer surface pressures of 105, 146 and 206 kPa, the peak positive pressures on the surface of the collagen gel were 10, 12, and 14 MPa, respectively (Figure 8a). The corresponding ARFs (ΔF/ΔV) on the collagen gels were found to be 0.93 x $10^6$, 4.65 x $10^6$, and 9.84 x $10^6$

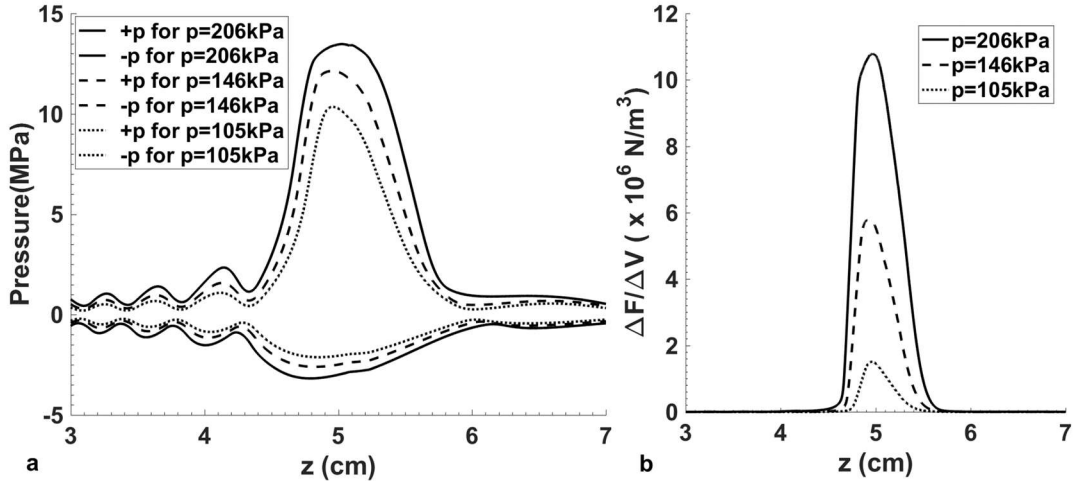


**Figure 8.** The axial peak positive and negative pressure as function of depth for various acoustic pressures (a), and ARF as a function of depth for various acoustic pressures (b). The acoustic pressures shown are the pressures on the surface of the transducer.

$Nm^{-3}$ for a transducer surface pressure of 105, 146 and 206 kPa, respectively (Figure 8b).

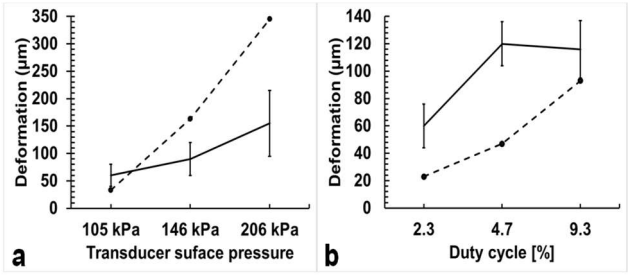


**Figure 9**. Comparison between the experimental US-induced gel deformation (solid line) and computational deformation from ARF induced pressure (dashed line). a) As function of acoustic pressure and duty cycle of 3.3%, and b) duty cycle and acoustic pressure of 105 kPa.

*2) Displacement of NPs*

In this study, we used PEBCA NPs with a diameter in the range of 140-195 nm (z-average), and density $1.48 g/cm^3$ [18]. The NPs will have a negligible extinction cross section because of their small size compared to the US wavelength (150 μm in water, at 10 MHz frequency) but can potentially be moved due to acoustic streaming. The acoustic streaming depends on the hydraulic conductivity, which also depends on viscosity. Using Eq. 8, the maximum displacement of the NPs as a function of transducer surface pressure and duty cycle are shown in Table. I. The results show that acoustic streaming under our conditions has very little effect on NP displacement.

TABLE I
MAXIMUM DISPLACEMENT OF NPS ESTIMATED BASED ON DARCY'S LAW WITH ($K' = 1.25x10^{-15}$ $M^4N^{-1}s^{-1}$ TO $10^{-13}$ $M^4N^{-1}s^{-1}$).

| Transducer surface pressure (kPa) | 105 | 146 | 206 | 105 | 105 | 105 |
|---|---|---|---|---|---|---|
| Duty cycle (%) | 3.3 | 3.3 | 3.3 | 2.33 | 4.67 | 9.33 |
| Maximum displacement of NPs (μm) | 0.02 –1.8 | 0.1 – 9.2 | 0.2 – 19.5 | 0.02 – 1.3 | 0.03 – 2.6 | 0.06– 5.2 |

*3) Deformation of collagen gel by US*

Two different pressure loads (ARF induced pressure and Langevin pressure) on the gel surface and their corresponding deformation were computed. Their corresponding deformations were estimated from Eq. 6. It was found that the ARF induced 14 to 69 times larger forces on the gel than Langevin pressure, which resulted in also 14 to 69 times larger deformation (see Appendix F, Figure S4).

The experimental US-induced deformation of the gel surface was compared to the numerical simulation of the deformation (Figure 9). The computed deformation was less than the experimental, except for the lowest pressure applied. This discrepancy is likely due to the experimental deformation being imaged some time (15-60 min) after US exposure and represents the plastic deformation, whereas the predicted deformation represents the elastic deformation immediately after US exposure.

To study the dynamic behavior of the gel due to compression, gel deformation induced by a mechanical load as well as the subsequent gel response when the load was removed, were imaged by CLSM (see Appendix G, Figure S5). The gel slowly restored for 10-14 minutes after the force was removed and reached plateau. 30-50% of the gel thickness was restored.

## IV. DISCUSSIONS

The composition and structure of the ECM in tumors can limit the movement of NPs within the tumor ECM [47, 48]. A collagen gel was developed that capture many of the material properties of the ECM. US has a potential to enhance the penetration of NPs and drugs through the ECM, but with the US parameters and gel parameters applied in the current study, no penetration of NPs into the gel was observed. Rather a deformation of the collagen gel corresponding to the lateral distribution of the US beam was observed. Computer simulations were consistent with the experimental data.

### *A. Characterization of collagen gels*

Collagen gel was used as a tissue-mimicking model as collagen gel displays several properties resembling ECM. Qualitatively, CRM showed that the collagen fibers in the gels were cross-linked in a network similar to tissue. The measured ADC value for the collagen gel (~$1.8 \times 10^{-3}$ $mm^2 s^{-1}$) is of the same order of magnitude as reported for five different xenograft tumors growing subcutaneously in athymic mice (~$0.6 \times 10^{-3}$ to $1 \times 10^{-3}$ $mm^2 s^{-1}$) [46]. The same MRI sequence was used in these tumor studies as used for the collagen gel. The ADC value of the collagen gel was somewhat higher than in tumors as expected from a model not containing cells, glycosaminoglycans and other proteins found in ECM in vivo. The mean free path of diffusing molecules in the collagen gels is therefore expected to be higher than *in vivo* ECM. This is consisted with clinical and animal studies which have shown that ADC is abnormal in tumors, and that elevated ADC reflects

an elevated non-cellular fraction [49], and ADC values decrease with increasing amount of collagen [50].

The Young modulus of the collagen gels was determined by macroindentation, and found to be 0.24 kPa, which is comparable to that reported by Valero et al (0.19 kPa for the same collagen concentration) [43]. The Young modulus for tumors containing 1-4% collagen is in the range of 0.66-39 kPa [51].

### B. PEGylation and diffusion of NPs in gels

PEGylation of NPs and surface charge are important for diffusion in gels [52] and tissue [53]. The close to neutral zeta potential of the NPs confirms a good coverage of PEG on the NP surface and will potentially reduce the interaction with the collagen network. However, the NPs could be divided into three populations: immobile, slow and fast diffusing indicating a subpopulation of "sticky" or adhesive NPs. The multimodal diffusion coefficient of NPs is likely to originate from the interactions with the heterogeneous distribution of components in the collagen matrix; regions of high collagen-fiber concentration and aqueous regions or pockets between the fibers, as seen in the two-phase nature of transport in the tumor matrix [54, 55]. It is likely that the fast component of diffusion is related to the NPs diffusing in aqueous pockets between collagen fibers, thereby the diffusion coefficient is approaching the diffusion coefficient in pure solution [54]. The slow and immobile NPs indicate electrostatic or other interactions between the NP and the collagen fibers. As we have previously reported for NPs of various PEGylation [21, 52], not only the PEGylation of the NPs determines the fraction of diffusing particles in a collagen matrix, but likely also the collagen polymerization which vary between samples. The collagen volume fraction and fiber size did qualitatively vary between samples and would affect the available aqueous pocket volume and hence the fraction of fast diffusing NPs, as seen in other studies [53, 56]. Experimental findings have shown that diffusion can be significantly hindered by electrostatic interactions between the diffusing particle and charged components of the ECM, as positive patches on the collagen fibers [57, 58]. Adding hyaluronic acid to the model (as found *in vivo* ECM) could with its negative charge shield the charge of the collagen to some extent and possibly decrease the interactions with NPs [59]. Another limiting factor to diffusing particles in our model is that NPs were added to collagen before polymerization. Possibly, the NPs can interfere more strongly with the collagen fibers before polymerization. This could also result in poorly polymerized collagen fibers and a higher collagen volume fraction in the gel, consisting of smaller collagen constituents rather than larger fibers.

### C. ARF on displacement of NPs

In an attempt to improve NP penetration in the gel, FUS was applied to the gels and depending on the acoustic pressures, the ARF was estimated to be in the order (0.93 - 9.84) x $10^6$ $Nm^{-3}$. ARF can act directly on the microsized particles and displace them, whereas NPs were hardly displaced [9], or acoustic streaming can be generated and translating NPs in the medium [40]. At 10 MHz, the US wavelength in water is approximately 150 μm whereas the size of NPs is approximately 177 nm. The small size of the NPs relative to the wavelength results in a negligible extinction cross section, and the dominant mechanism is most likely acoustic streaming. Both the experimental and computational approach showed insignificant (nm to μm range) penetration of NPs, indicating that acoustic streaming was not large enough to produce a significant transport of the NPs in the collagen gel. Computational simulations resulted in a maximum of 20 μm displacement of NPs into the gel at the highest pressure applied and assuming high gel hydraulic conductivity.

One explanation for this short displacement is the low acoustic attenuation of the collagen gel (approximately 0.64 dB/cm at 10 MHz), resulting in a relatively small ARF. Thus, in future studies, one should use gels that absorb more acoustic energy by adding cells, higher concentrations of collagen, glycosaminoglycans for instance hyaluronan, or other absorbing molecules. Another limitation in our experiments is the low pressures and duty cycle that could be applied to avoid damage of the transducer. The insignificant NP penetration could be caused by NPs being trapped in the collagen gel if the size of the NPs is larger than pore size or if NPs are adhering to the collagen fibers. Thus, a larger ARF that can push the NPs or alter the collagen network might be required to overcome such hindrance.

The particle density has shown to have an impact on US-induced displacement of NPs [40]. NPs of diameter 200 nm and density of 1.41 $gcm^{-3}$ ($SiO_2$) were found to penetrate approximately 100 μm into the gel due to potentially ARF and acoustic streaming at center frequency of 1 MHz. However, cavitation activity was detected although no microbubbles were added, and cavitation could have influenced the NP penetration. In our study, cavitation activity is unlikely to take place with the frequency and US parameters used, and theoretically the NPs could penetrate only 20 μm into the gel assuming high hydraulic conductivity. At the highest pressure applied, the mechanical index, which describes the likelihood of cavitation activity, was found to be 0.95. This is below the value where cavitation can be expected [7].

### D. ARF on deformation of the collagen gel

The US applied caused deformation of the collagen gel, and the width of the deformation on the collagen surface corresponded to the US beam. The deformation increased with applied acoustic pressure and duty cycle, which is consistent with previous studies [30, 60]. However, when the duty cycle was further increased from 4.7% to 9.3%, the deformation of the collagen gel did not become larger, and unfortunately the transducer did not allow us to increase the duty cycle further. The deformation of the gel decreased exponentially with the position into the gel.

The deformation of the gel caused by ARF was estimated both experimentally and computationally and approximately two times larger deformation was found computationally for the highest pressures used. A possible explanation is that the

deformation was measured sometime after the US exposure, thus we observed the permanent plastic deformation. Imaging the restoration of the collagen gel during and after unloading the indenter, revealed that the gel reached 30-50% of its thickness 10 min after unloading the indenter, demonstrating that the gel obtained a permanent deformation. Thus, the plastic deformation we observed after US exposure will be less than the computed deformation that determined the maximum deformation immediately after US exposure. This is consistent with plastic behavior of the gel reported when subjecting collagen networks to compression [61-63] and tension [64].

The observed deformation of the collagen gel could be caused by a combination of ARF due to absorption and ARF due to reflection or Langevin pressure. ARF due to absorption appeared to be the dominant mechanism. Depending on the acoustic pressure applied, ARF due to absorption was estimated to be 14 to 69 times larger than deformation induced by Langevin pressure.

## V. Conclusion

The characterization of the collagen gel shows that such gels have important characteristics in common with the ECM of tissue, and gel models are an important complementary approach to studies in mice. However, the overall conclusion is that the penetration of NPs due to the applied ARF and possible acoustic streaming is negligible in this collagen gel model. It also shows that ARF caused by absorption rather than reflection is the dominant mechanism for the deformation of the collagen gel. Although ARF was not found to improve the penetration of NPs into ECM, using gels with higher acoustic attenuation which can be achieved by adding cells, more collagen, glycosaminoglycans or other absorbing molecules. Also applying higher acoustic intensities and duty cycles, might give different results, and should be a follow-up study.

## Appendix

### A. Surface pressure of US transducer

One circular single element US transducer was selected for the experiment based on initial simulations of ARF. The transducer was selected from the Olympus high-power Immersion series, and has a center frequency of 10 MHz with diameter of 19 mm and focused at 50 mm. The transmitted field of the US transducer was measured prior to the experiment. The transducer was immersed in a water tank measurement system (Onda AIMS-III), and the pressure was recorded with an HGL-0085 hydrophone (Onda Corporation, Sunnyvale, CA, USA) using an AH-2020 pre-amplifier (Onda Corporation, Sunnyvale, CA, USA). The beam profile in the focal plane was recorded with a low excitation voltage to avoid damage to the hydrophone. The pressure was recorded in a 2D grid in the focal plane with a lateral resolution of 0.1 mm.

Simulation was used to estimate the ARF generated with the parameters used in the experiment. One important input parameter in the simulations was the surface pressure, which was estimated with the following procedure. First, the total acoustic transmission power was estimated in water and in a 2D measurement plane at 5 mm in front of the focus. This was conducted using a low excitation voltage (11 Vpp) to ensure that the combined effects of non-linear distortion and limited hydrophone bandwidth did not corrupt the measurements. The lateral resolution in the 2D grid was 0.1 mm, and the grid sizes were 2×2 mm, which were large enough to capture the -20 dB beam width of the transducer. The transmitted power was subsequently distributed evenly over the surface of the transducer, assuming plane wave approximations at the measurement grid and at the transducer surface. Furthermore, assuming negligible absorption in water, the transducer surface pressure was estimated as;

$$p_{S,\mathrm{ref}} \approx \sqrt{\frac{2\Delta x \Delta y f_c}{A_S N_p f_s} \sum_i \sum_j \sum_n |p(i,j,z_1,n)|^2} \qquad \text{(A.1)}$$

where $p(i,j,z_1,n)$ is the pressure measurement at the grid point $(i,j)$ in the 2D measurement plane at $z_1$, and $n$ is the temporal sample number. The terms $\Delta x$ and $\Delta y$ are the lateral resolutions in the 2D measurement grid, $f_s$ is the temporal sampling frequency, $f_c$ is the center frequency of the transmitted pulse, $N_P$ is the number of cycles in the transmitted pulse, and $A_S$ is the aperture of the transducer. This formula was used to calculate the reference surface pressure at a low excitation voltage.

The estimation of the surface pressure at a higher excitation voltage using the described technique is challenging due to the increased amount of harmonic distortion, which causes the power spectral density of the pulse to be non-zero outside the calibration range of the hydrophone. Close to the transducer, there is negligible harmonic distortion, regardless of the excitation voltage, since harmonic distortion is an accumulative effect. However, the pressure amplitude at a given point in the near-field varies linearly with the surface pressure. Therefore, the near-field pressure was measured using a) the excitation voltage that was used to calculate the surface pressure in Eq. (A.1) and b) the excitation voltages used in the mouse experiments. The surface pressure at higher excitation voltage was then estimated by the following:

$$p_S(V_{ext}) = p_{S,ref}\frac{p_0(V_{ext})}{p_{0,ref}} \quad (A.2)$$

where $p_0(V_{ext})$ is the near filed pressure at different excitation voltages, $p_{S,ref}$ is the reference surface pressure estimated using Eq. (A.1), and $p_{0,ref}$ is the near-field pressure measured at the same excitation voltage as $p_{S,ref}$.

### B. Acoustic Radiation Force (ARF)

The ARF on a small volume, $\Delta V$, is given by the transfer of momentum from a passing wave to the volume. Let $\boldsymbol{u} = \boldsymbol{u}(\boldsymbol{r}, \boldsymbol{t})$ be the vibration velocity vector field at the position $\boldsymbol{r}$, and $\rho$ be the density of the volume $\Delta V$. The radiation force on the volume is given by

$$F_r(r) = -\int_V \rho \frac{1}{T}\int_0^T \boldsymbol{u}\nabla.\boldsymbol{u} + (\boldsymbol{u}.\nabla)\boldsymbol{u}\, dt\, dV \quad (B.1)$$

where the time $T$ is the duration of the passing wave. Assuming that over the small volume the passing wave can be approximated as a plane wave, the vibration velocity vector field is approximated by $\boldsymbol{u} \approx u\boldsymbol{e}_z$ where $\boldsymbol{e}_z$ is the unit normal along the z-axis. The integrand of Eq. (B.1) simplifies to

$$\boldsymbol{u}\nabla.\boldsymbol{u} + (\boldsymbol{u}.\nabla)\boldsymbol{u} = 2u\frac{du}{dz}\boldsymbol{e}_z \quad (B.2)$$

For a plane, progressive wave, the pressure is related to the vibration velocity by the characteristic impedance, $Z = \rho c$, where $c$ is the propagation velocity in the medium. It is also known that the attenuation of a plane progressive wave is

$$\frac{dI(\boldsymbol{r},\omega)}{dz} = -\sigma_e(\boldsymbol{r},w)I(r,w) \rightarrow \frac{dP(\boldsymbol{r},\omega)}{dz} = -\frac{1}{2}\alpha(\boldsymbol{r},\omega)P(\boldsymbol{r},\omega) \quad (B.3)$$

where $I(\boldsymbol{r},w)$ is the temporal Fourier transform of the instantaneous intensity, $P(\boldsymbol{r},\omega)$ is the temporal Fourier transform of the pressure, and $\alpha(\boldsymbol{r},\omega)$ is the attenuation, and is the sum of absorption and scattering. Substituting $p(\boldsymbol{r},t) = \rho c\, u(\boldsymbol{r},t)$ into Eq. (B.2), and inserting into Eq. (B.1), the expression for the ARF becomes

$$F_r(r) = -\rho\frac{2e_z}{T(\rho c)^2}\int_V\int_0^T p(\boldsymbol{r},t)\,\frac{dp(\boldsymbol{r},t)}{dz}\,dt\,dV \quad (B.4)$$

Using Plancherel's theorem, the ARF is

$$F_r(r) = -\frac{2e_z}{2\pi T\rho c^2}\int_V\int_{-\infty}^{\infty} P(r,\omega)\,\frac{dP(r,\omega)}{dz}\,d\omega\,dV \quad (B.5)$$

Finally, inserting Eq. (B.3), and letting the ARF be uniform over the volume $\Delta V$, the ARF per unit volume can be expressed as

$$\frac{F_r(\boldsymbol{r})}{\Delta V} = \frac{\boldsymbol{e}_z}{2\pi T\rho c^2}\int_{-\infty}^{\infty}\alpha(\boldsymbol{r},\omega)|P(\boldsymbol{r},\omega)|^2\,d\omega \quad (B.6)$$

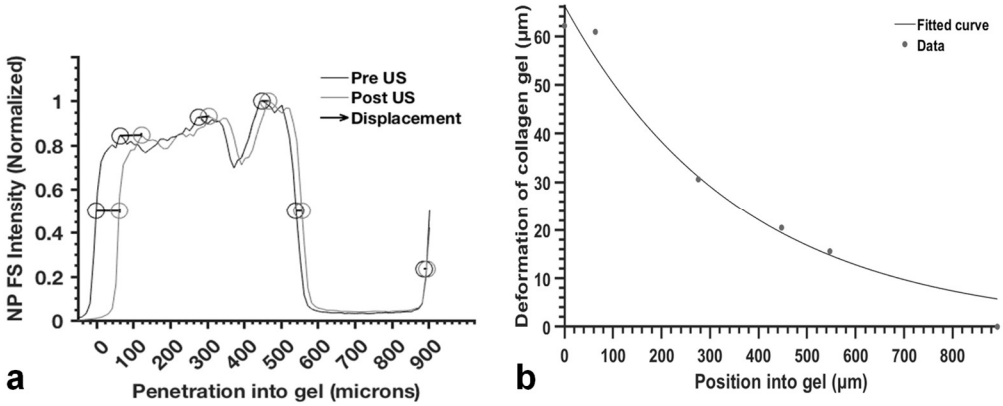


**Figure S1:** Example of data analysis (2.2MPa (at the focus) US treatment): The intensity profile of NP fluorescence plotted as a function of penetration depth into the gel pre and post US (black and gray curves respectively in a). The fluorescence intensity profile is characterized by two regions: the NP-collagen layer (first 500 μm) with a high fluorescence level and the collagen-only layer (next 400 μm) with a close to zero fluorescence level. In this analysis example, five points along the curves were used to calculate the NP displacement, two half maximum intensity points and three additional points (indicated by black and grey circles along the curve). From the difference in opposition in the gel of these five points between pre to post US intensity curves, the NP displacement was calculated and plotted as a function of penetration into the gel as shown in b) along with the best fitted trending curve, an exponential decay function. FS= fluorescence.

### *C. Quantification of gel deformation and NPs penetration*

The mean intensity profiles obtained before and after US exposure were treated separately as they were normalized to their maximum value and the auto fluorescence was set to zero. The resulting intensity profiles were plotted as mean normalized intensity as a function of depth into the collagen gel, Figure S1. The fluorescence intensity is close to zero in the PBS solution above the gel surface, increases when entering the NP-collagen layer and drops towards zero in the interface between the NP-collagen/collagen gel (around 500 µm into the gel). The steep intensity increases at the end of the intensity profile (around 900 µm into the gel) was originating from the cover slip and was used to align the two curves.

### *D. Estimation for Young's modulus of collagen gels*

The Young modulus was determined from indentation data, and the Hertz contact model was fitted to the experimental data. The first 100-120 µm of the indentation depth to the gel thickness was selected to estimate Young's modulus of the collagen. A representative experimental indentation curve and the corresponding fitting are shown in Figure S2.

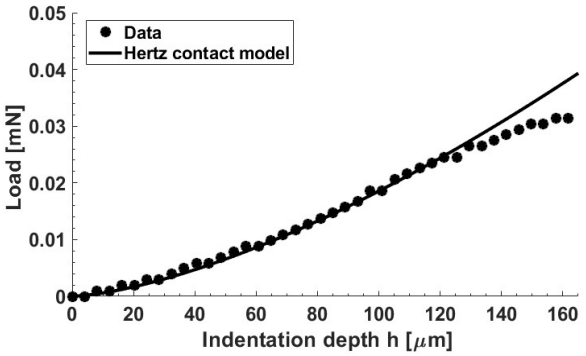


**Figure S2.** Representative load-distance curve. Hertz contact model was used for fitting and estimating Young modulus of the collagen

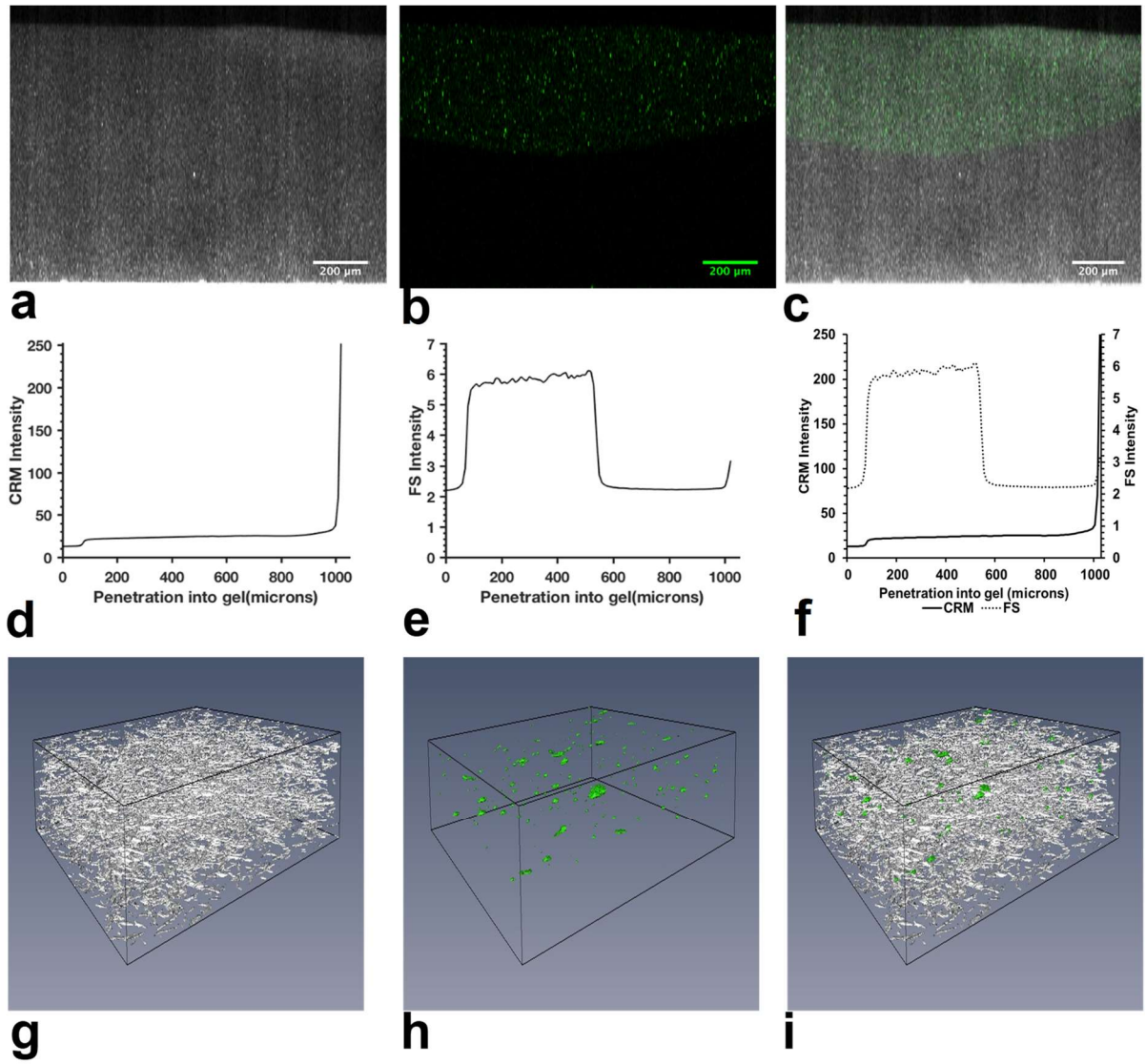


**Figure S3:** Gel images. First row shows an orthogonal view of a XZ cross section of the imaged region of the gel; from the PBS solution above the gel surface to the well plate, image dimensions: 1030x1367 (h x w). a) Reflection channel, b) Fluorescence channel, c) overlay image both channels. The second row, d) ,e) and f), shows the intensity profile as a function of penetration into the gel corresponding to the images in a), b) and c), respectively. The third row shows a 3D reconstruction of a Z-stack of a 38x38x80 µm (w x l x h) selected area at the boundary between the two layers in the model; g) collagen fibers (white), h) NPs (green) i) overlay between collagen fibers (white) and NPs (green).CRM= confocal reflection microscopy, FS= fluorescence.

### *E. Two-layered collagen tissue-mimicking model*

Two-layer collagen tissue mimicking ECM model where NPs were only in the first layer was designed. Examples images are shown in Figure S3. Figure S3a-c, shows orthogonal views of a XZ cross section of the gel for the reflection channel (Figure S3a), the fluorescence channel (Figure S3b) and an overlay image (Figure S3c). The corresponding intensity profiles for the three 3D image stacks are shown in Figure S3d –f. The intensity profile of the reflection channel (Figure S3d) is mainly from collagen, and shows a close to constant intensity, which implies a continuous fiber network in the gel with crosslinking of the fibers throughout the gel. No peaks that would originate from a boundary or discontinuous collagen crosslinking are observed. The intensity profile of the fluorescence channel (Figure S3e) is mainly from NPs and shows a step increase in the fluorescence intensity corresponding to the gel surface and a step reduction in the fluorescence representing the boundary between the NP-collagen and collagen only layers. In Figure S3g-i, a 3D reconstruction visualizes the collagen fibers, NP cluster distribution and an overlay image respectively, from a volume of 38x38x80 µm (w x l x h) at the boundary between the two layers.

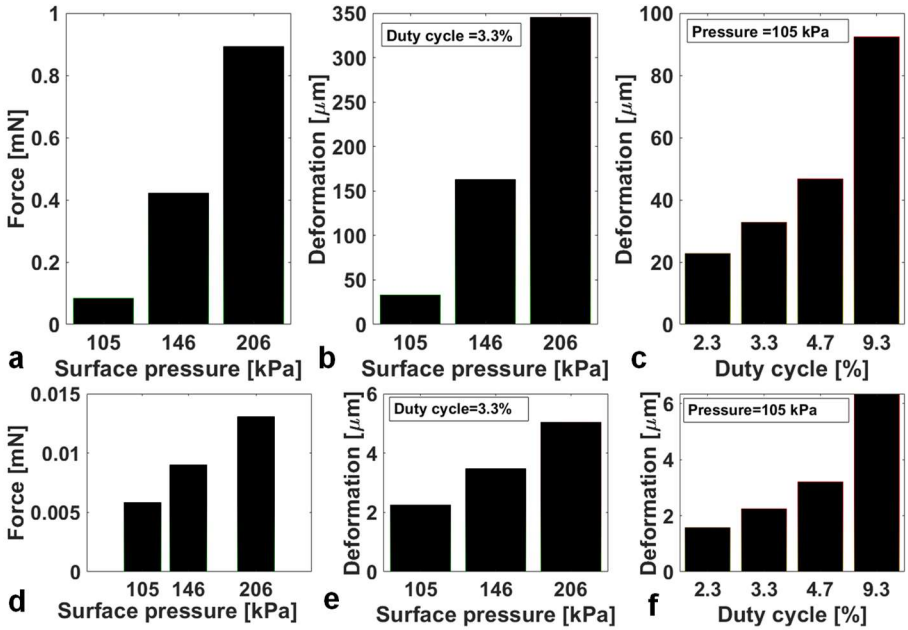


**FigureS4**: Forces due to ARF on the gel estimated from the simulation (a) and their corresponding deformations estimated for various acoustic pressures (b), and different duty cycles (c). Forces due to Langevin pressure on the gel estimated from the simulation (d) and their corresponding deformations estimated for various acoustic pressures (e), and different duty cycles (f).

### *F. Comparing simulated gel deformation by ARF and Langevin pressure*

The observed gel deformation can be caused by the propagating US wave being absorbed in the gel, which we call ARF or reflected between two media called Langevin radiation force. These two forces and their corresponding deformation of the gel is shown in figure S4. ARF is clearly much larger than the Langevin radiation pressure and causes much larger deformation.

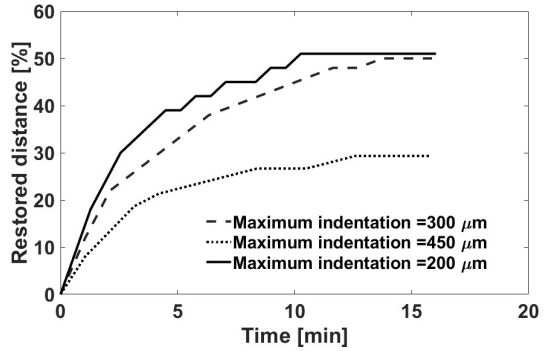


**Figure S5.** Collagen gel restoration. The three plots show number of experiments. Zero time corresponds to the uploading of the indenter. The gel was compressed for 2 minutes and recorded the CRM image of the collagen gel while uploading the load. The restored displacement of the gel as function of time was measured.

### *G. Estimation of collagen gel restoration*

One layer collagen gel (2.5 mg/ml) was placed in a container with diameter of 18 mm and height of 2 mm, and 40 µl of PBS was added on top of the gel to avoid drying. The macroindenter (a spherical tip diameter of 0.6 mm) compressed the collagen gel reducing its thickness 20-25% (indentation 200-450 um), and the indenter compressed the gel for 2 min before being unloaded. CRM z stack images of the collagen gel were recorded while unloading the indenter and continued recording for approximately 15 minutes. From the recorded images, the percentage of the restored distance of the collagen gel was estimated. Two different collagen samples were used for the study.

The results are shown in Figure S5, and show that only 30-50% of the gel thickness was restored within 15 minutes after removing the indenter.


## ACKNOWLEDGMENT

RC acknowledge the support of The Oxford Centre for Drug Delivery Devices (OxCD3) and the Engineering and Physical Sciences Research Council (EPSRC). Anne Rein Hatletveit (SINTEF) is acknowledged for producing NPs.

## REFERENCES


[1] J. Fang, H. Nakamura, and H. Maeda, "The EPR effect: Unique features of tumor blood vessels for drug delivery, factors involved, and limitations and augmentation of the effect," *Adv. Drug Deliv. Rev.,* vol. 63, pp. 136-151, Mar. 2011.

[2] H. Maeda, J. Wu, T. Sawa, Y. Matsumura, and K. Hori, "Tumor vascular permeability and the EPR effect in macromolecular therapeutics: a review," *J. Control. Release,* vol. 65, pp. 271-284, Mar. 2000.

[3] S. Wilhelm, A. J. Tavares, Q. Dai, S. Ohta, J. Audet, H. F. Dvorak*, et al.*, "Analysis of nanoparticle delivery to tumours," *Nat. Rev. Mater.,* vol. 1, p. 16014, 2016.

[4] C. d. L. Davies, L. M. Lundstrøm, J. Frengen, L. Eikenes, Ø. S. Bruland, O. Kaalhus*, et al.*, "Radiation Improves the Distribution and Uptake of Liposomal Doxorubicin (Caelyx) in Human Osteosarcoma Xenografts," *Cancer Res.,* vol. 64, p. 547, Jan. 2004.

[5] S. Eggen, M. Afadzi, E. A. Nilssen, S. B. Haugstad, B. Angelsen, and C. d. L. Davies, "Ultrasound Improves the Uptake and Distribution of Liposomal Doxorubicin in Prostate Cancer Xenografts," *Ultrasound Med. Biol.,* vol. 39, pp. 1255-1266, Jul. 2013.

[6] Z. Izadifar, P. Babyn, and D. Chapman, "Mechanical and Biological Effects of Ultrasound: A Review of Present Knowledge," *Ultrasound Med. Biol.,* vol. 43, pp. 1085-1104, Jun. 2017.

[7] D. Dalecki, "Mechanical Bioeffects of Ultrasound," *Annu. Rev. Biomed. Eng.,* vol. 6, pp. 229-248, Aug. 2004.

[8] K. Nightingale, M. S. Soo, R. Nightingale, and G. Trahey, "Acoustic radiation force impulse imaging: in vivo demonstration of clinical feasibility," *Ultrasound Med. Biol.,* vol. 28, pp. 227-235, Feb. 2002.

[9] P. A. Dayton, S. Zhao, S. H. Bloch, P. Schumann, K. Penrose, T. O. Matsunaga*, et al.*, "Application of Ultrasound to Selectively Localize Nanodroplets for Targeted Imaging and Therapy," *Mol. Imaging,* vol. 5, p. 7290.2006.00019, Jul. 2006.

[10] P. A. Dayton, K. E. Morgan, A. L. Klibanov, G. Brandenburger, K. R. Nightingale, and K. W. Ferrara, "A preliminary evaluation of the effects of primary and secondary radiation forces on acoustic contrast agents," *IEEE Transactions on Ultrasonics, Ferroelectrics, and Frequency Control,* vol. 44, pp. 1264-1277, Nov. 1997.

[11] P. A. Dayton, K. E. Morgan, A. L. Klibanov, G. H. Brandenburger, and K. W. Ferrara, "Optical and acoustical observations of the effects of ultrasound on contrast agents," *IEEE Transactions on Ultrasonics, Ferroelectrics, and Frequency Control,* vol. 46, pp. 220-232, Jan. 1999.

[12] A. F. H. Lum, M. A. Borden, P. A. Dayton, D. E. Kruse, S. I. Simon, and K. W. Ferrara, "Ultrasound radiation force enables targeted deposition of model drug carriers loaded on microbubbles," *J. Control. Release,* vol. 111, pp. 128-134, Mar. 2006.

[13] P. Dayton, A. Klibanov, G. Brandenburger, and K. Ferrara, "Acoustic radiation force in vivo: a mechanism to assist targeting of microbubbles," *Ultrasound Med. Biol.,* vol. 25, pp. 1195-1201, Oct. 1999.

[14] M. J. Shortencarier, P. A. Dayton, S. H. Bloch, P. A. Schumann, T. O. Matsunaga, and K. W. Ferrara, "A method for radiation-force localized drug delivery using gas-filled lipospheres," *IEEE Transactions on Ultrasonics, Ferroelectrics, and Frequency Control,* vol. 51, pp. 822-831, Aug. 2004.

[15] V. Frenkel, E. Kimmel, and Y. Iger, "Ultrasound-induced intercellular space widening in fish epidermis," *Ultrasound Med. Biol.,* vol. 26, pp. 473-480, Mar. 2000.

[16] D. S. Hersh, B. A. Nguyen, J. G. Dancy, A. R. Adapa, J. A. Winkles, G. F. Woodworth*, et al.*, "Pulsed ultrasound expands the extracellular and perivascular spaces of the brain," *Brain Res.,* vol. 1646, pp. 543-550, Sep. 2016.

[17] R. Raghavan, "Theory for acoustic streaming in soft porous matter and its applications to ultrasound-enhanced convective delivery," *Journal of Therapeutic Ultrasound,* vol. 6, p. 6, Aug. 2018.

[18] Ý. Mørch, R. Hansen, S. Berg, A. K. O. Åslund, W. R. Glomm, S. Eggen*, et al.*, "Nanoparticle-stabilized microbubbles for multimodal imaging and drug delivery," *Contrast Media Mol. Imaging,* vol. 10, pp. 356-366, Sep. 2015.

[19] A. S. Klymchenko, E. Roger, N. Anton, H. Anton, I. Shulov, J. Vermot*, et al.*, "Highly lipophilic fluorescent dyes in nano-emulsions: towards bright non-leaking nano-droplets," *RSC Adv,* vol. 2, pp. 11876-11886, Oct. 2012.

[20] S. Snipstad, S. Berg, Ý. Mørch, A. Bjørkøy, E. Sulheim, R. Hansen*, et al.*, "Ultrasound Improves the Delivery and Therapeutic Effect of Nanoparticle-Stabilized Microbubbles in Breast Cancer Xenografts," *Ultrasound Med. Biol.,* vol. 43, pp. 2651-2669, Nov. 2017.

[21] A. K. O. Åslund, E. Sulheim, S. Snipstad, E. von Haartman, H. Baghirov, N. Starr*, et al.*, "Quantification and Qualitative Effects of Different PEGylations on Poly(butyl cyanoacrylate)

Nanoparticles," *Mol. Pharm.,* vol. 14, pp. 2560-2569, Feb. 2017.

[22] J. Cebulla, E. M. Huuse, K. Pettersen, A. van der Veen, E. Kim, S. Andersen*, et al.*, "MRI reveals the in vivo cellular and vascular response to BEZ235 in ovarian cancer xenografts with different PI3-kinase pathway activity," *Br. J. Cancer,* vol. 112, p. 504, Dec. 2014.

[23] X. Li, Y. H. An, Y.-D. Wu, Y. C. Song, Y. J. Chao, and C.-H. Chien, "Microindentation test for assessing the mechanical properties of cartilaginous tissues," *Journal of Biomedical Materials Research Part B: Applied Biomaterials,* vol. 80B, pp. 25-31, May 2007.

[24] T. Jin, L. Li, R. C. M. Siow, and K.-K. Liu, "A novel collagen gel-based measurement technique for quantitation of cell contraction force," *Journal of The Royal Society Interface,* vol. 12, May 2015.

[25] P. J. Rae and D. M. Dattelbaum, "The properties of poly(tetrafluoroethylene) (PTFE) in compression," *Polymer,* vol. 45, pp. 7615-7625, Oct. 2004.

[26] Z. Hamrang, A. Pluen, E. Zindy, and D. J. J. o. p. s. Clarke, "Raster image correlation spectroscopy as a novel tool for the quantitative assessment of protein diffusional behaviour in solution," *J. Pharm. Sci.,* vol. 101, pp. 2082-2093, Feb. 2012.

[27] D. Stalling, M. Westerhoff, and H.-C. J. T. v. h. Hege, "Amira: A highly interactive system for visual data analysis," *The visualization handbook,* vol. 38, pp. 749-67, 2005.

[28] J. A. Rooney and W. L. Nyborg, "Acoustic Radiation Pressure in a Traveling Plane Wave," *Am J Phys,* vol. 40, pp. 1825-1830, 1972.

[29] G. R. Torr, "The acoustic radiation force," *American Journal of Physics,* vol. 52, pp. 402-408, May 1984.

[30] J. R. Doherty, G. E. Trahey, K. R. Nightingale, and M. L. Palmeri, "Acoustic radiation force elasticity imaging in diagnostic ultrasound," *IEEE Transactions on Ultrasonics, Ferroelectrics, and Frequency Control,* vol. 60, pp. 685-701, Mar. 2013.

[31] T. L. Szabo, "Chapter 4 - Attenuation," in *Diagnostic Ultrasound Imaging: Inside Out (Second Edition)*, ed Boston: Academic Press, 2014, pp. 81-119.

[32] J. E. Soneson, "A User-Friendly Software Package for HIFU Simulation," *AIP Conference Proceedings,* vol. 1113, pp. 165-169, Apr. 2009.

[33] T. L. Szabo, "Chapter 12 - Nonlinear Acoustics and Imaging," in *Diagnostic Ultrasound Imaging: Inside Out (Second Edition)*, ed Boston: Academic Press, 2014, pp. 501-563.

[34] K. P. Mercado, M. Helguera, D. C. Hocking, and D. Dalecki, "Noninvasive Quantitative Imaging of Collagen Microstructure in Three-Dimensional Hydrogels Using High-Frequency Ultrasound," *Tissue Engineering. Part C, Methods,* vol. 21, pp. 671-682, Mar. 2015.

[35] S. A. Goss and F. Dunn, "Ultrasonic propagation properties of collagen," *Phys. Med. Biol.,* vol. 25, p. 827, Sep. 1980.

[36] B. A. J. Angelsen, *Ultrasound imaging: waves, signals, and signal processing*. Trondheim: Emantec AS, 2000.

[37] R. Grapenthin, "CrusDe: A plug-in based simulation framework for composable Crustal Deformation studies using Green's functions," *Computers & Geosciences,* vol. 62, pp. 168-177, Jan. 2014.

[38] H. Geirsson, T. Árnadóttir, C. Völksen, W. Jiang, E. Sturkell, T. Villemin*, et al.*, "Current plate movements across the Mid-Atlantic Ridge determined from 5 years of continuous GPS measurements in Iceland," *Journal of Geophysical Research: Solid Earth,* vol. 111, Sep. 2006.

[39] P. A. Dayton, K. W. Ferrara, S. Zhao, H. Zheng, R. Zutshi, P. Schumann*, et al.*, "1F-4 Acoustic Localization of Sub-Micron Droplets for Targeted Imaging and Therapy," in *2006 IEEE Ultrasonics Symposium*, 2006, pp. 521-524.

[40] L.-B. Harriet, T. Boon, S. Eleanor, and C. C. Constantin, "The effect of particle density on ultrasound-mediated transport of nanoparticles," *Phys. Med. Biol.,* vol. 61, p. 7906, Oct. 2016.

[41] P. A. Netti, L. T. Baxter, Y. Boucher, R. Skalak, and R. K. Jain, "Time-dependent behavior of interstitial fluid pressure in solid tumors: implications for drug delivery," *Cancer Res.,* vol. 55, pp. 5451-8, Nov. 1995.

[42] E. A. Swabb, J. Wei, and P. M. Gullino, "Diffusion and Convection in Normal and Neoplastic Tissues," *Cancer Res.,* vol. 34, pp. 2814-2822, Oct. 1974.

[43] C. Valero, H. Amaveda, M. Mora, and J. M. García-Aznar, "Combined experimental and computational characterization of crosslinked collagen-based hydrogels," *PLoS One,* vol. 13, pp. e0195820-e0195820, Apr. 2018.

[44] M. A. Swartz and M. E. Fleury, "Interstitial Flow and Its Effects in Soft Tissues," *Annu. Rev. Biomed. Eng.,* vol. 9, pp. 229-256, Aug. 2007.

[45] S. Park, C. Whittington, S. L. Voytik-Harbin, and B. Han, "Microstructural parameter-based modeling for transport properties of collagen matrices," *J. Biomech. Eng.,* vol. 137, pp. 061003-061003, Jun. 2015.

[46] E. Sulheim, J. Kim, A. van Wamel, E. Kim, S. Snipstad, I. Vidic*, et al.*, "Multi-modal characterization of vasculature and nanoparticle accumulation in five tumor xenograft models," *J. Control. Release,* vol. 279, pp. 292-305, Jun. 2018.

[47] C. d. L. Davies, D. A. Berk, A. Pluen, and R. K. Jain, "Comparison of IgG diffusion and extracellular matrix composition in rhabdomyosarcomas grown in mice versus in vitro as spheroids reveals the role of host stromal cells," *Br. J. Cancer,* vol. 86, p. 1639, May 2002.

[48] P. A. Netti, D. A. Berk, M. A. Swartz, A. J. Grodzinsky, and R. K. Jain, "Role of Extracellular Matrix Assembly in Interstitial Transport in Solid Tumors," *Cancer Res.,* vol. 60, p. 2497, May 2000.

[49] R. Sinkus, B. E. Van Beers, V. Vilgrain, N. DeSouza, and J. C. J. E. j. o. c. Waterton, "Apparent diffusion coefficient from magnetic resonance imaging as a

biomarker in oncology drug development," *Eur. J. Cancer Clin. Oncol.,* vol. 48, pp. 425-431, Mar. 2012.

[50] A. Hauge, C. S. Wegner, J.-V. Gaustad, T. G. Simonsen, L. M. K. Andersen, and E. K. Rofstad, "Diffusion-weighted MRI-derived ADC values reflect collagen I content in PDX models of uterine cervical cancer," *Oncotarget,* vol. 8, p. 105682, Dec. 2017.

[51] J. Liu, H. Zheng, P. S. P. Poh, H.-G. Machens, and A. F. Schilling, "Hydrogels for Engineering of Perfusable Vascular Networks," *Int. J. Mol. Sci.,* vol. 16, p. 15997, Jul. 2015.

[52] S. Lélu, S. P. Strand, J. Steine, and C. d. L. J. B. Davies, "Effect of PEGylation on the diffusion and stability of chitosan–DNA polyplexes in collagen gels," *Biomacromolecules,* vol. 12, pp. 3656-3665, Aug. 2011.

[53] T. Stylianopoulos, M.-Z. Poh, N. Insin, M. G. Bawendi, D. Fukumura, L. L. Munn*, et al.*, "Diffusion of particles in the extracellular matrix: the effect of repulsive electrostatic interactions," *Biophys. J.,* vol. 99, pp. 1342-1349, Sep. 2010.

[54] G. Alexandrakis, E. B. Brown, R. T. Tong, T. D. McKee, R. B. Campbell, Y. Boucher*, et al.*, "Two-photon fluorescence correlation microscopy reveals the two-phase nature of transport in tumors," *Nat. Med.,* vol. 10, p. 203, Jan. 2004.

[55] V. P. Chauhan, R. M. Lanning, B. Diop-Frimpong, W. Mok, E. B. Brown, T. P. Padera*, et al.*, "Multiscale measurements distinguish cellular and interstitial hindrances to diffusion in vivo," *Biophysical journal,* vol. 97, pp. 330-336, Jul. 2009.

[56] E. B. Brown, Y. Boucher, S. Nasser, and R. K. J. M. r. Jain, "Measurement of macromolecular diffusion coefficients in human tumors," *Microvasc. Res.,* vol. 67, pp. 231-236, May 2004.

[57] O. Lieleg, R. M. Baumgärtel, and A. R. J. B. j. Bausch, "Selective filtering of particles by the extracellular matrix: an electrostatic bandpass," *Biophys. J.,* vol. 97, pp. 1569-1577, Sep. 2009.

[58] R. G. Thorne, A. Lakkaraju, E. Rodriguez-Boulan, and C. J. P. o. t. N. A. o. S. Nicholson, "In vivo diffusion of lactoferrin in brain extracellular space is regulated by interactions with heparan sulfate," *PNAS,* vol. 105, pp. 8416-8421, Jun. 2008.

[59] J. Lam, N. F. Truong, and T. J. A. b. Segura, "Design of cell–matrix interactions in hyaluronic acid hydrogel scaffolds," *Acta Biomater.,* vol. 10, pp. 1571-1580, Apr. 2014.

[60] K. Nightingale, M. S. Soo, R. Nightingale, R. Bentley, D. Stutz, M. Palmeri*, et al.*, "Acoustic radiation force impulse imaging: remote palpation of the mechanical properties of tissue," in *2002 IEEE Ultrasonics Symposium, 2002. Proceedings.*, 2002, pp. 1821-1830

[61] E. A. Abou Neel, U. Cheema, J. C. Knowles, R. A. Brown, and S. N. Nazhat, "Use of multiple unconfined compression for control of collagen gel scaffold density and mechanical properties," *Soft Matter,* vol. 2, pp. 986-992, Oct. 2006.

[62] P. L. Chandran and V. H. Barocas, "Microstructural Mechanics of Collagen Gels in Confined Compression: Poroelasticity, Viscoelasticity, and Collapse," *J. Biomech. Eng.,* vol. 126, pp. 152-166, Apr. 2004.

[63] D. M. Knapp, V. H. Barocas, A. G. Moon, K. Yoo, L. R. Petzold, and R. T. Tranquillo, "Rheology of reconstituted type I collagen gel in confined compression," *Journal of Rheology,* vol. 41, pp. 971-993, Sep. 1997.

[64] M. E. Susilo, J. A. Paten, E. A. Sander, T. D. Nguyen, and J. W. Ruberti, "Collagen network strengthening following cyclic tensile loading," *Interface Focus,* vol. 6, p. 20150088, Feb. 2016.